

Towards High-Performance Solid-State-LiDAR-Inertial Odometry and Mapping

Kailai Li, Meng Li, and Uwe D. Hanebeck

*Intelligent Sensor-Actuator-Systems Laboratory (ISAS)
Institute for Anthropomatics and Robotics
Karlsruhe Institute of Technology (KIT), Germany
emails: kailai.li@kit.edu, uyjjl@student.kit.edu, uwe.hanebeck@kit.edu*

Abstract

We present a novel tightly-coupled LiDAR-inertial odometry and mapping scheme for both solid-state and mechanical LiDARs. As frontend, a feature-based lightweight LiDAR odometry provides fast motion estimates for adaptive keyframe selection. As backend, a hierarchical keyframe-based sliding window optimization is performed through marginalization for directly fusing IMU and LiDAR measurements. For the Livox Horizon, a newly released solid-state LiDAR, a novel feature extraction method is proposed to handle its irregular scan pattern during preprocessing. LiLi-OM (Livox LiDAR-inertial odometry and mapping) is real-time capable and achieves superior accuracy over state-of-the-art systems for both LiDAR types on public data sets of mechanical LiDARs and in experiments using the Livox Horizon. Source code and recorded experimental data sets are available on Github¹.

1. Introduction

Estimating six-DoF egomotion plays a fundamental role in a wealth of applications ranging from robot navigation and inspection to virtual/augmented reality, see [1, 2, 3, 4, 5]. With the booming of autonomous driving, light detection and ranging (LiDAR) sensors have gained tremendous popularity [6, 7]. Compared to visual sensors, 3D LiDARs provide lighting-invariant and accurate perception of the surroundings with long detection range and high robustness. Thus, they are broadly deployed to mobile agents for odometry and mapping.

Essentially, LiDAR-based odometry requires computing six-DoF egomotion given consecutive frames of point clouds. This can be performed via scan-matching algorithms, e.g., via the iterative closest point (ICP) [8] method. Instead of directly using downsampled raw point clouds, features representing local geometries are extracted for scan-matching. In [9], planar patches are extracted to perform ICP with a point-to-plane metric. This was further generalized in [10], where a plane-to-plane metric was proposed for improved robustness.

3D LiDARs for mobile perception usually have a large output streaming volume at a typical frequency of 10Hz. In most application scenarios, real-time processing is required, albeit given limited onboard computing resources. Thus, much attention has been dedicated to feature-based scan-matching [11, 12, 13]. In [14], features are extracted from object edges and planes for scan-matching using point-to-edge and point-to-plane metrics, which enables accurate LiDAR-based odometry in real time. In [15], an image-based segmentation approach was applied to feature extraction [16] and the same metrics in [14] were used. Furthermore, a two-stage optimization scheme was tailored for ground vehicles to enable light-weight LiDAR odometry and mapping.

In principle, LiDAR point clouds perceived from a mobile agent are distorted due to its egomotion. In addition, output frequency of the data stream is relatively low. Consequently, performance of

¹<https://github.com/KIT-ISAS/lili-om>

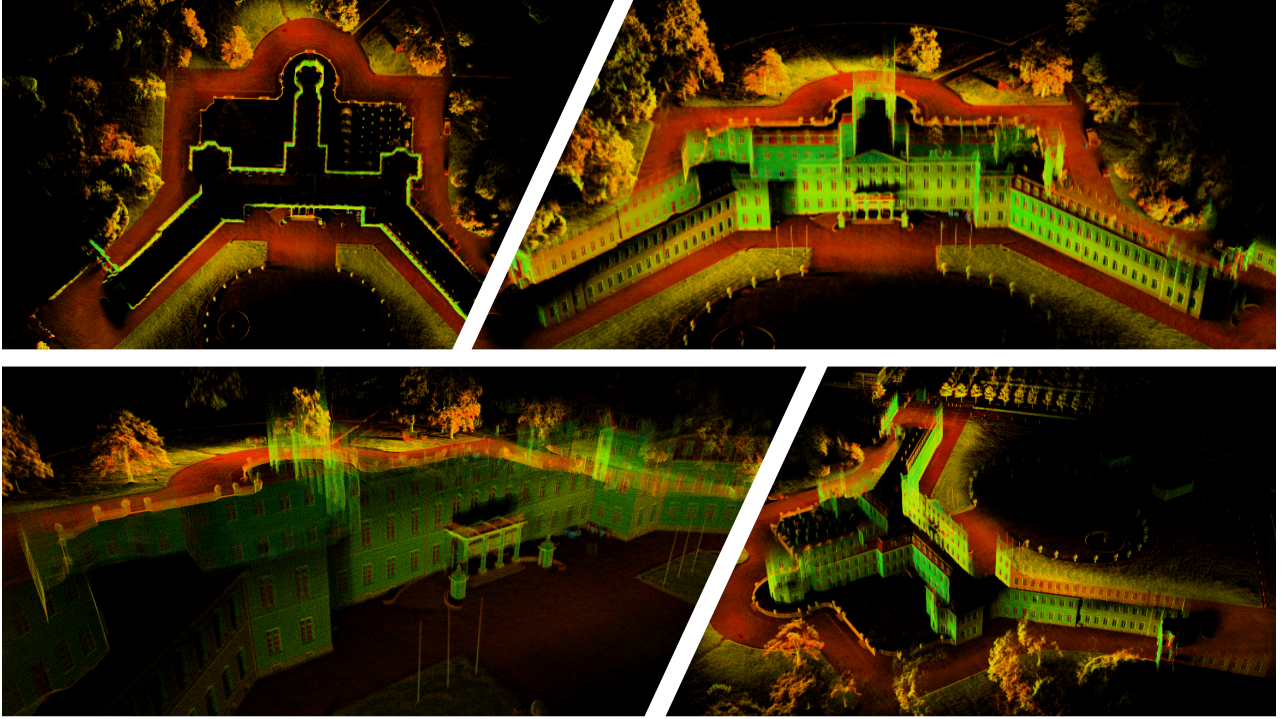


Figure 1: 3D map of Schloss Karlsruhe from LiLi-OM.

LiDAR-only odometry is prone to deterioration under fast motion or in complex scenes. Inertial sensors, however, provide instant motion information at much higher frequencies and can bridge the gap between consecutive LiDAR frames. Therefore, integrating inertial sensors has become crucial for robust and accurate LiDAR-based egomotion estimation. In [14, 15], an inertial measurement unit (IMU) was incorporated for de-skewing raw point clouds and for providing prior motion estimates for scan-matching-based LiDAR odometry. Decoupled schemes are appealing to save computational resources and apply classic filtering methods, e.g., the extend Kalman filter (EKF). However, loosely coupled fusion schemes may lead to information loss and inaccurate estimates [17].

This leads to an increasing focus on tightly-coupled LiDAR-inertial odometry, where IMU and point cloud measurements are fused in a joint optimization or filtering framework. Here, pre-integrated IMU readings are often employed for de-skewing per-frame LiDAR scanning [18]. In [19], an optimization-based approach was proposed for LiDAR-inertial odometry with a maximum a posteriori (MAP) formulation incorporating both the LiDAR and IMU residuals in a sliding window fashion. An additional method using rotational constraints was proposed to refine the final pose and map, which delivers similar or better tracking accuracy as [14]. However, real-time processing is hard to achieve in practice as sensor readings of every frame are exploited.

To improve the runtime efficiency of LiDAR-inertial odometry, an iterated error-state Kalman filter was introduced in [20] based on a robocentric formulation. It runs in real time and shows superior tracking accuracy over existing LiDAR-only odometry systems. In [21], a tightly-coupled LiDAR-inertial odometry system was proposed based on the incremental smoothing and mapping framework iSAM2 [22]. However, the system relies heavily on [14] to produce LiDAR odometry factors to further constrain the pre-integrated IMU states in the factor graph formulation. Unlike direct fusion of IMU and LiDAR measurements within a unified scheme, this can result in loss of constraint information posed by landmarks. Also, correlations between LiDAR and IMU measurements might be largely discarded. To guarantee high odometry accuracy, the system requires nine-axis IMU readings of high frequency (500Hz as used in [21]) to de-skew the point cloud and initialize LiDAR odometry. Fusion with additional sensor modalities (e.g., GPS signals) is often needed at certain spots to achieve precise localization.

More importantly, LiDARs of conventional design rely on mechanical spinning mechanisms to enable 360-degree FoV, however, with a quite limited vertical resolution. Few LiDARs with high vertical resolution have emerged on the market, e.g., Hesai Pandar-128² and Velodyne VLS-128³. However, their extremely high prices have been prohibitive for mass market supply of robotics industry and research.

Very recently, *solid-state LiDARs* have hit the consumer market based on various working principles with much better affordability. Existing solid-state LiDARs often have non-repetitive and irregular scan patterns. Also, they have relatively small FoVs to reach uniform and high resolution. So far, solid-state-LiDAR-based odometry has not been well investigated. In [23], a conventional LiDAR odometry system [14] was adapted to Livox Mid-40⁴, a solid-state LiDAR with a circular FoV of 38.4°. Here, feature extraction and scan-matching are done similarly to [14]. Compared with the baseline in [14], it produces comparable tracking accuracy with improved runtime efficiency due to parallelization. To the best of the authors’ knowledge, no published research on tightly-coupled LiDAR-inertial odometry systems using solid-state LiDARs exists to date.

In this paper, we provide a specific study on solid-state-LiDAR-inertial odometry and mapping. Instead of the Livox Mid-40, we choose the Livox Horizon that was newly released in the first quarter of 2020. It is designed for mobile perception and especially autonomous cars⁵ with a FoV of 81.7° × 25.1°. Scanning at 10 Hz, it reaches a similar coverage as a typical 64-line mechanical LiDAR with much more uniform density. Also, it is substantially cheaper than most existing 3D LiDARs of comparable performance.

Scan patterns of solid-state LiDARs are always irregular and non-repetitive, so that common feature extraction methods for conventional 3D LiDARs, e.g., in [14, 15], are not applicable. For example, extracting features along incident and deflection angles as in [23] is impossible for the Livox Horizon, as it sweeps in a totally unstructured and irregular pattern⁶. Such a pattern is more generic for reaching broader FoV with uniform coverage, which can potentially become common for future generation solid-state LiDARs. Compared to conventional 3D LiDARs, however, solid-state LiDARs have limited FoV, making it tricky to perform odometry in some circumstances, especially under fast motion or with insufficient features.

Contributions

Considering the state-of-the-art research above and 3D LiDAR evolution, we propose a novel tightly-coupled LiDAR-inertial odometry and mapping scheme with a specific variant for solid-state LiDARs (pipeline in Sec. 2). A novel feature extraction approach is tailored to the irregular scan pattern of the Livox Horizon (Sec. 3). To directly fuse LiDAR and IMU measurements in a unified manner, a hierarchical keyframe-based fusion scheme is proposed using sliding window optimization (Sec. 4). The proposed system is generically applicable for both conventional and the deployed solid-state LiDARs. It runs in real time and delivers superior odometry and mapping accuracy over related state-of-the-art systems (Sec. 5). We publish the new solid-state-LiDAR-inertial data sets recorded by Livox Horizon and Xsens MTi-670. The code of the proposed system is open-source under LiLi-OM (Livox LiDAR-Inertial Odometry and Mapping). Thanks to the low hardware costs and real-time performance on mobile platforms, it provides a cost-effective solution for robot perception in various scenarios.

2. System Pipeline

The proposed LiDAR-inertial odometry and mapping scheme is shown in Fig. 2. The 3D LiDAR (e.g., Livox Horizon) streams out point clouds at a typical frequency of 10 Hz and is synchronized

²<https://www.hesai.tech.com/en/Pandar128>

³<https://velodynelidar.com/products/alpha-prime>

⁴<https://www.livoxtech.com/mid-40-and-mid-100>

⁵<https://www.livoxtech.com/de/horizon>

⁶Scanning of Mid-40 is specially regularized to form a circular coverage.

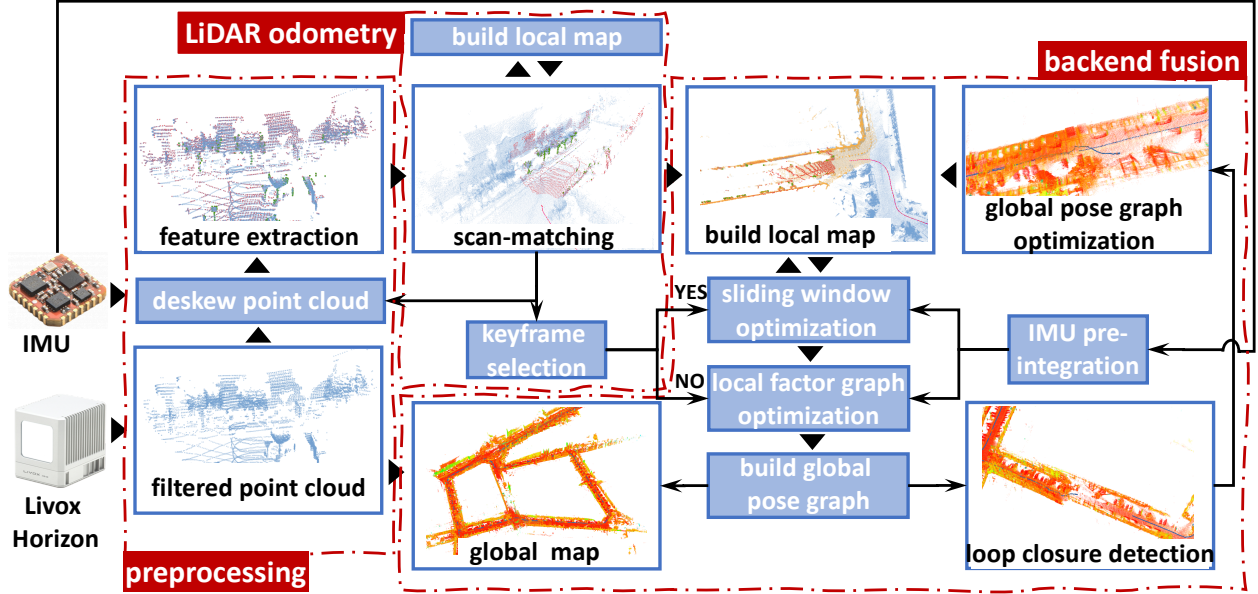


Figure 2: Pipeline of the proposed LiDAR-inertial odometry and mapping system.

with a six-axis IMU providing gyroscope and accelerometer readings at higher frequency (e.g., 200 Hz for Xsens MTi-670⁷). We want to simultaneously estimate six-DoF egomotion of the LiDAR frame and a globally consistent map. The raw point clouds from LiDAR scanning are first downsampled and rotationally de-skewed using gyroscope data. Then, feature points representing planes (red) and edges (green) are extracted (Sec. 3.1). Given the preprocessed scans, a light-weight scan-matching-based odometry module runs in a frame-to-model manner for fast motion estimation with point-to-edge and point-to-plane metrics being exploited (Sec. 3.2). The relative motion estimates of consecutive LiDAR frames are further used to de-skew the translational part of the current LiDAR feature sweep. Besides, keyframes are selected adaptively to the perceived scene transition given the estimated relative motion. Parallel to the preprocessing and LiDAR odometry nodes, the backend module directly fuses LiDAR and IMU measurements in a unified manner via the proposed keyframe-based sliding window optimization in Sec. 4.

The fusion window usually covers several (e.g., three) keyframes. As the window slides, keyframe states (denoted with \checkmark on top as follows) are optimized in the current window

$$\checkmark \mathbf{x}_k = [\checkmark \mathbf{t}_k^\top, \checkmark \mathbf{v}_k^\top, \checkmark \mathbf{q}_k^\top, \checkmark \mathbf{b}_k^\top]^\top \in \mathbb{R}^3 \times \mathbb{R}^3 \times \mathbb{S}^3 \times \mathbb{R}^6 \subset \mathbb{R}^{16}. \quad (1)$$

Here, $\checkmark \mathbf{t}_k \in \mathbb{R}^3$ and $\checkmark \mathbf{q}_k \in \mathbb{S}^3$ denote the keyframe position and orientation (represented by unit quaternions), respectively. $\checkmark \mathbf{v}_k \in \mathbb{R}^3$ is the velocity and $\checkmark \mathbf{b}_k = [\checkmark \mathbf{b}_{k,a}^\top, \checkmark \mathbf{b}_{k,g}^\top]^\top \in \mathbb{R}^6$ denotes the term incorporating the IMU bias of the accelerometer (subscript ‘a’) and the gyroscope (subscript ‘g’). After being slid over, optimized keyframes of consecutive order are used as constraints to optimize the in-between regular-frame poses via factor graph optimization. A global pose graph is maintained to incorporate all poses of LiDAR frames. Loop closure is checked in a keyframe basis, and when necessary, a global graph optimization is invoked to guarantee the reconstructed map to be globally consistent.

3. Feature-Based Solid-State LiDAR Scan-Matching

3.1. Feature extraction for irregular scan pattern

Existing 3D solid-state LiDARs often have non-repetitive and irregular scan patterns. Thus, popular methods of extracting geometric features, e.g., in [14, 15], are not applicable. The approach

⁷<https://www.xsens.com/products/mti-600-series>

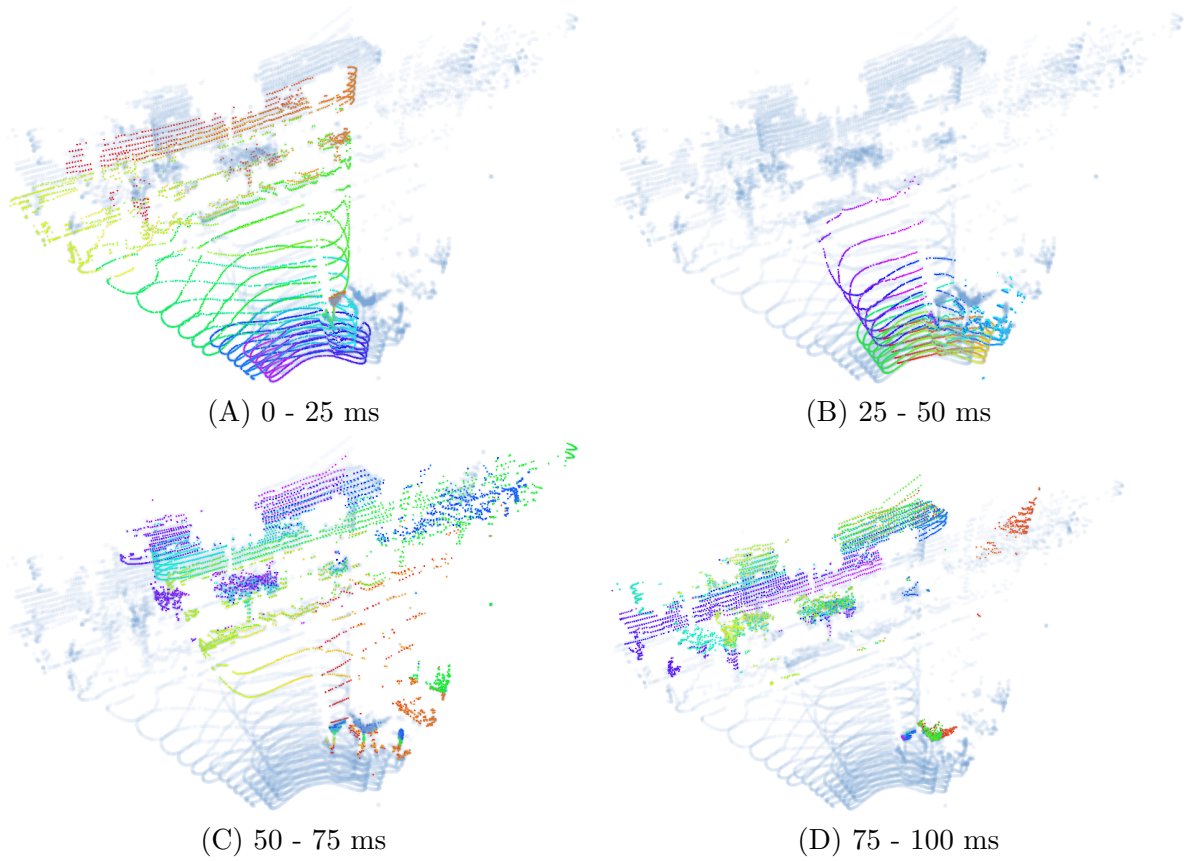


Figure 3: Scan pattern of the Livox Horizon. Points are rendered according to time stamps with rainbow color scale.

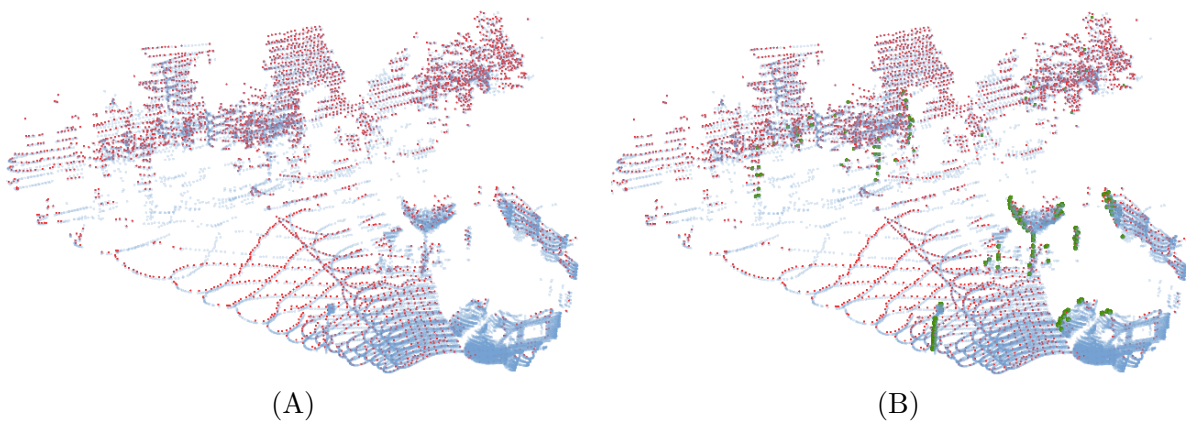


Figure 4: Illustration of feature extraction for points scanned by the Livox Horizon. Given one sweep (blue blots), plane features are first extracted (red dots) in (A), after which edge features are extracted (green dots) in (B).

in [23] for the Livox Mid-40 is not appropriate for the Horizon because the Mid-40 has a structured scan pattern of circular shape. The newly released Livox Horizon, however, has a totally different and more generic scan pattern with its multi-laser sensing module. An array of six vertically-aligned laser diodes sweeps back and forth through the prisms with an arbitrary “brushing” pattern in the $81.7^\circ \times 25.1^\circ$ FoV. We show one frame of scanning (10 Hz frequency) from the Livox Horizon in Fig. 3. The whole sweep of 100 ms is divided into four stages for illustration. The six points from the multi-laser transceiver are vertically aligned and perceived simultaneously, and thus, are rendered as the same color. In one sweep, the six-head “brush” scans non-repetitively in the space, reaching an area coverage within the FoV via integration over time per frame.

The 3D resolution of the Livox Horizon is much more uniform than that of conventional LiDARs with repetitive scan patterns. To extract features from planes and edges from the point cloud of Livox Horizon, we propose a new two-stage approach. Shown in Alg. 1, we unfold the per-frame sweep in its time domain, where 6×7 -point patches are assigned one after another (Alg. 1, line 2). In each patch \mathbb{P}_i , we perform eigendecomposition of the covariance of the 3D coordinates of the 42 points⁸ (Alg. 1, line 4-5). If the second largest eigenvalue is substantially larger than the smallest one (e.g., $\lambda_1/\lambda_2 < 0.3$), then points in the patch are extracted as surface features (Alg. 1, line 6-7). For non-surface patches, we search the point with largest curvature on each scan line and perform eigendecomposition for the six points (Alg. 1, line 8-14). If the largest eigenvalue is substantially larger than the second largest one (e.g., $\lambda_2/\lambda_3 < 0.25$), then the points form a line and they are extracted as edge features (Alg. 1, line 15-16).

We show an example of extracted features from one frame of the Livox Horizon point cloud in Fig. 4. Note that the proposed feature extraction algorithm is purely performed in the time domain of every sweep given time stamps of the perceived point array. This is radically different from the approaches in [14, 23] that compute local smoothness on each scan line for structured scan pattern. Furthermore, we associate each feature point with its corresponding edge’s direction vector or plane’s normal vector to represent local geometries. It will be further exploited to weight the LiDAR residual in the backend fusion module.

3.2. Point-to-edge and point-to-plane metric

Given the extracted edge and plane features, both the frontend odometry module and the sliding window optimization for backend fusion in Fig. 2 exploit the scan-matching formulation to incorporate LiDAR measurements for egomotion estimation. Following metrics are applied.

Point-to-edge metric

Suppose an edge feature $\mathbf{p}_k^\ell \in \mathbb{E}$ is extracted from sweep \mathbb{W} w.r.t. the LiDAR frame ℓ and its associated unit vector $\boldsymbol{\nu}_e$ indicating the edge direction is available. We first search its nearest five edge points in the corresponding local feature map \mathbb{M}^ω and compute their coordinates’ mean value $\bar{\mathbf{e}}^\omega$ and covariance matrix (w.r.t. the global frame ω). Based thereon, an eigendecomposition is performed. If the largest eigenvalue is significantly larger than the rest, the five points in \mathbb{M}^ω form a line with its direction vector \mathbf{n}_e being the eigenvector corresponding to the largest eigenvalue. We then take two points $\hat{\mathbf{e}}^\omega = \bar{\mathbf{e}}^\omega + \delta \mathbf{n}_e$ and $\hat{\mathbf{e}}^\omega = \bar{\mathbf{e}}^\omega - \delta \mathbf{n}_e$ on the fitted line and exploit a point-to-edge metric of the following form

$$\mathcal{D}_e(\mathbf{x}_k^\omega, \mathbf{p}_k^\ell, \mathbb{M}^\omega) = \frac{\|(\mathbf{p}_k^\omega - \hat{\mathbf{e}}^\omega) \times (\mathbf{p}_k^\omega - \hat{\mathbf{e}}^\omega)\|}{\|\hat{\mathbf{e}}^\omega - \hat{\mathbf{e}}^\omega\|}.$$

Here, $\mathbf{p}_k^\omega = \mathbf{q}_k \otimes \mathbf{p}_k^\ell \otimes \mathbf{q}_k^\circ + \mathbf{t}_k$ denotes the scan point w.r.t., the global frame given current LiDAR pose $\mathbf{x}_k^\top = [\mathbf{q}_k^\top, \mathbf{t}_k^\top]^\top$. \otimes denotes the Hamilton product and \mathbf{q}_k° the conjugate of the unit quaternion \mathbf{q}_k . Typically, $\delta = 0.1$.

⁸At most 42 points are considered as some of them might be addressed with inconcrete readings.

Algorithm 1: Feature Extraction for Livox Horizon

Input: single sweep \mathbb{W}
Output: edge feature set \mathbb{E} , plane feature set \mathbb{F}

```
1  $\mathbb{E} \leftarrow \emptyset, \mathbb{F} \leftarrow \emptyset;$   
2  $\{\mathbb{P}_i = \{\mathbf{X}_r\}_{r=1}^6 \mid \mathbf{X}_r \in \mathbb{R}^{3 \times 7}\}_{i=1}^\tau \leftarrow \text{split}(\mathbb{W});$   
3 for  $i \leftarrow 1$  to  $\tau$  do  
4    $\Sigma_i \leftarrow \text{getCovariance}(\mathbb{P}_i);$   
5    $\{(\lambda_1, \lambda_2, \lambda_3)\} \leftarrow \text{eig}(\Sigma_i);$  //  $\lambda_1 \leq \lambda_2 \leq \lambda_3$   
   /* check plane feature */  
6   if  $\lambda_1/\lambda_2 < 0.3$  then  
7      $\mathbb{F} \leftarrow \mathbb{F} \cup \mathbb{P}_i;$   
8   else  
   /* check edge feature */  
9      $\mathbb{G}_i \leftarrow \emptyset;$   
10    for  $r \leftarrow 1$  to 6 do  
11       $\mathbf{x}_r \leftarrow \text{getCurv}(\mathbf{X}_r);$   
12       $\mathbb{G}_i \leftarrow \mathbb{G}_i \cup \mathbf{X}_r;$   
13     $\Gamma_i \leftarrow \text{getCovariance}(\mathbb{G}_i);$   
14     $\{(\lambda_1, \lambda_2, \lambda_3)\} \leftarrow \text{eig}(\Gamma_i);$   
15    if  $\lambda_2/\lambda_3 < 0.25$  then  
16       $\mathbb{E} \leftarrow \mathbb{E} \cup \mathbb{G}_i;$ 
```

Point-to-plane metric

If the feature point \mathbf{p}_k^ℓ indicates a plane (with a normal $\boldsymbol{\nu}_s$), we also transform it into its world coordinates \mathbf{p}_k^w and find its nearest five plane feature points in the corresponding local feature map w.r.t. the global frame, namely $\mathbb{S}^w = \{\mathbf{s}_j^w\} \subset \mathbb{M}^w$, with $j = 1, \dots, 5$. We solve an overdetermined linear equation $\mathbf{A}_s \mathbf{u}_s = \mathbf{c}$ via QR decomposition. Here, $\mathbf{A}_s = [\mathbf{s}_1^w, \dots, \mathbf{s}_5^w] \in \mathbb{R}^{5 \times 3}$ and $\mathbf{c} = [-1, \dots, -1] \in \mathbb{R}^5$. The desired normal vector can be obtained via $\mathbf{n}_s = \mathbf{u}_s / \|\mathbf{u}_s\|$. Then, the point-to-plane metric can be established as

$$\mathcal{D}_s(\mathbf{x}_k^w, \mathbf{p}_k^\ell, \mathbb{M}^w) = \mathbf{n}_s^\top (\mathbf{q}_k \otimes \mathbf{p}_k^\ell \otimes \mathbf{q}_k^\circ + \mathbf{t}_k) + 1 / \|\mathbf{u}_s\| .$$

3.3. Metric weighting function

In order to quantify the contribution of each LiDAR residual during sensor fusion, we propose a metric weighting function according to the association quality as follows

$$\mathcal{W}_\circ(\mathbf{p}_k^\ell) = \lambda \cdot (\boldsymbol{\nu}_\circ)^\top \mathbf{n}_\circ \cdot \exp\left(-\sum_{j=1}^5 |\gamma(\mathbf{p}_k^\ell) - \gamma_j|\right) . \quad (2)$$

Here, \circ indicates the type of feature correspondences, namely edges (subscript ‘e’) or surfaces (subscript ‘s’). For an edge feature correspondence, $\boldsymbol{\nu}_e$ and \mathbf{n}_e denote the direction vector of the edge line at \mathbf{p}_k^ℓ and the line approximated by its nearest five edge features, respectively. Similarly, $\boldsymbol{\nu}_s$ and \mathbf{n}_s denote the surface normal at point \mathbf{p}_k^ℓ and the one formed by its nearest five surface features, respectively. Moreover, $\gamma(\mathbf{p}_k^\ell)$ and γ_j are the reflectance values of the feature point \mathbf{p}_k^ℓ and its associated nearest five features, respectively. Typically, we have the constant $\lambda = 15$. Therefore, the proposed metric weighting function considers both geometric and appearance consistencies of feature associations.

4. Tightly-Coupled LiDAR-Inertial Fusion via Keyframe-Based Sliding Window Optimization

4.1. Keyframe-based fusion hierarchy

Keyframe-based schemes have originally been proposed and widely applied to visual odometry for achieving accurate tracking with real-time performance [24]. In [21], keyframe poses from the

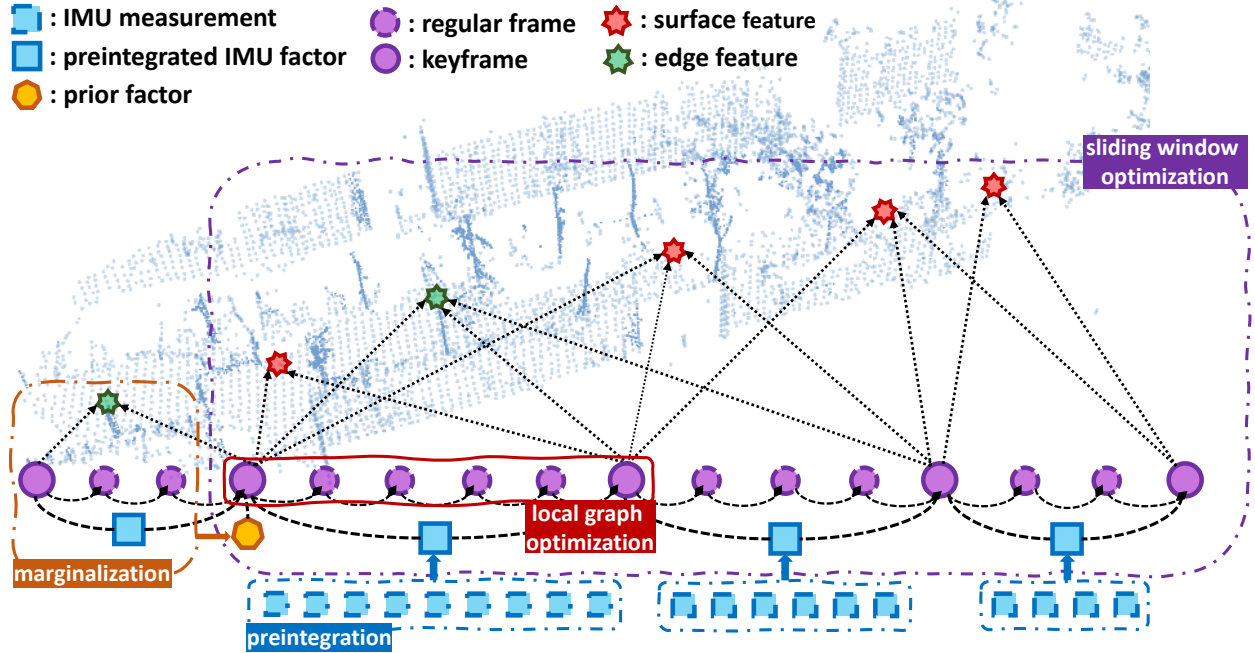


Figure 5: Proposed tightly-coupled LiDAR-inertial fusion scheme using keyframe-based sliding window optimization.

LiDAR odometry frontend [15] are fused to constrain IMU factors via iSAM2 (thus indirect fusion). The tightly-coupled LiDAR-inertial odometry system in [19] realized direct fusion of LiDAR and pre-integrated IMU measurements via sliding window optimization. However, real-time performance is not generally achievable as the scheme fuses LiDAR sweeps of every frame.

Therefore, it is of importance to maintain the sparsity of the optimization scheme for direct LiDAR-inertial fusion at the backend. Shown in Fig. 5, the proposed fusion scheme exploits keyframes to establish sliding windows, where LiDAR and pre-integrated IMU measurements are fused in a unified manner via nonlinear optimization. Setting up keyframes can critically affect odometry accuracy due to the IMU drift during the time interval of two consecutive keyframes. We introduce two criteria for keyframe selection: (1) If the overlapping ratio between features of the current frame and the local feature map is smaller than 60% or (2) if the time difference to the last keyframe is more than a certain number of (e.g., two) regular frames, the current frame is then selected as a new keyframe. As the window slides forward after optimization, we construct a local factor graph incorporating the two oldest keyframe poses as constraints and the regular frames poses initialized by IMU measurements. A small-scale factor graph optimization is invoked to obtain regular-frame poses at LiDAR sampling frequency.

4.2. Sliding window optimization for keyframes

We compute keyframe states of form (1) by solving a nonlinear optimization problem incorporating LiDAR features and pre-integrated IMU measurements, all observed at keyframes in a sliding window. We use a maximum a-posterior (MAP) objective function incorporating three components, i.e.,

$$\mathcal{J}(\check{\mathbf{X}}) = \|\mathcal{R}_{\mathcal{P}}(\check{\mathbf{X}})\|^2 + \sum_{k=1}^{\tau_w} \sum_{i=1}^m \|\mathcal{R}_{\mathcal{L}}(\check{\mathbf{x}}_k^w, \check{\mathbf{p}}_{k,i}^{\ell}, \check{\mathbf{M}}^w)\|^2 + \sum_{k=1}^{\tau_w} \|\mathcal{R}_{\mathcal{I}}(\check{\mathbf{x}}_k, \hat{\mathbf{z}}_{k+1}^k)\|_{\mathbf{C}_{k+1}^k}^2. \quad (3)$$

Here, $\check{\mathbf{X}} = [\check{\mathbf{x}}_1^{\top}, \dots, \check{\mathbf{x}}_{\tau_w}^{\top}]^{\top} \in \mathbb{R}^{15 \times \tau_w}$ denotes the concatenated keyframe states in the sliding window with τ_w being the window width. $\mathcal{R}_{\mathcal{P}}(\check{\mathbf{X}})$ denotes the prior term representing the measurements that are marginalized out due to window-sliding. The LiDAR residual term $\mathcal{R}_{\mathcal{L}}(\check{\mathbf{x}}_k^w, \check{\mathbf{p}}_{k,i}^{\ell}, \check{\mathbf{M}}^w)$ is induced by aligning the observed feature $\check{\mathbf{p}}_{k,i}^{\ell}$ w.r.t. the keyframe pose $\check{\mathbf{x}}_k^w$ to $\check{\mathbf{M}}^w$, a local map

combining the recent keyframes of observed features (typically 30 keyframes), and m is the number of associations. Furthermore, $\mathcal{R}_{\mathcal{S}}(\check{\mathbf{x}}_k, \hat{\mathbf{z}}_{k+1}^k)$ is the residual of IMU constraints at keyframe k with $\hat{\mathbf{z}}_{k+1}^k$ being pre-integrated IMU measurements from keyframe k to $k+1$. Details about the three components follow.

Prior factor

In order to bound the computational burden for LiDAR-inertial fusion without substantial information loss, we exploit marginalization in the keyframe-based window. Here, the oldest keyframe and its measurements are marginalized out via the Schur-complement [25]. A new prior is computed accordingly and added on top of the existing prior factor to carry the estimate from the removed keyframe to the next window.

LiDAR residual

Given the metrics and weighting function in Sec. 3.2, geometric constraints from LiDAR measurements can be incorporated into the fusion scheme. For that, the following residual term is established

$$\mathcal{R}_{\mathcal{L}}(\check{\mathbf{x}}_k, \check{\mathbf{p}}_k, \check{\mathbb{M}}^w) = \begin{cases} \tilde{W}_e(\check{\mathbf{p}}_k) \mathcal{D}_e(\check{\mathbf{x}}_k, \check{\mathbf{p}}_k, \check{\mathbb{M}}^w), & \check{\mathbf{p}}_k \in \check{\mathbb{E}}_k^\ell \\ \tilde{W}_s(\check{\mathbf{p}}_k) \mathcal{D}_s(\check{\mathbf{x}}_k, \check{\mathbf{p}}_k, \check{\mathbb{M}}^w), & \check{\mathbf{p}}_k \in \check{\mathbb{F}}_k^\ell \end{cases}.$$

Here, \mathcal{D}_e and \mathcal{D}_s are the point-to-edge and point-to-plane metrics, respectively. \tilde{W}_e and \tilde{W}_s denote normalized values of corresponding weights among all existing correspondences.

IMU measurement residual

We compute the IMU residual term in a similar way as [25, 19] using a quaternion representation of spatial orientation. To avoid repropagating IMU states each time the optimization window slides, raw inertial readings are pre-integrated between two consecutive keyframes k and $k+1$. Based thereon, the residual term incorporating the IMU constraints is established at keyframes, namely,

$$\mathcal{R}_{\mathcal{I}}(\check{\mathbf{x}}_k, \hat{\mathbf{z}}_{k+1}^k) = \begin{bmatrix} \check{\mathbf{R}}_k^{w\top} (\check{\mathbf{t}}_{k+1}^w - \check{\mathbf{t}}_k^w + \frac{1}{2} \mathbf{g}^w \Delta\tau_k^2 - \mathbf{v}_k^w \Delta\tau_k) - \hat{\boldsymbol{\alpha}}_{k+1}^k \\ \check{\mathbf{R}}_k^{w\top} (\check{\mathbf{v}}_{k+1}^w + \mathbf{g}^w \Delta\tau_k - \check{\mathbf{v}}_k^w) - \hat{\boldsymbol{\beta}}_{k+1}^k \\ 2[(\mathbf{q}_k^w)^{-1} \otimes \mathbf{q}_{k+1}^w \otimes (\hat{\boldsymbol{\gamma}}_{k+1}^k)^{-1}]_{2:4} \\ \check{\mathbf{b}}_{a,k+1} - \check{\mathbf{b}}_{a,k} \\ \check{\mathbf{b}}_{g,k+1} - \check{\mathbf{b}}_{g,k} \end{bmatrix}.$$

$\Delta\tau_k$ denotes the time interval between consecutive keyframes k and $k+1$. We use the operator $[\cdot]_{2:4}$ to take out the last three elements of a quaternion vector. $\hat{\mathbf{z}}_{k+1}^k = [\hat{\boldsymbol{\alpha}}_{k+1}^{k\top}, \hat{\boldsymbol{\beta}}_{k+1}^{k\top}, \hat{\boldsymbol{\gamma}}_{k+1}^{k\top}]^\top$ is the pre-integrated IMU measurements incorporating gyroscope and accelerometer readings from keyframe k to $k+1$. Due to space constraints, we do not provide the derivation of IMU pre-integration and the corresponding noise covariance \mathbf{C}_{k+1}^k for the Mahalanobis norm in (3). A dedicated introduction can be found in [25].

Based on the proposed objective function in (3), keyframe states in the current sliding window can be obtained via $\check{\mathbf{X}}^* = \arg \min_{\check{\mathbf{X}}} \mathcal{J}(\check{\mathbf{X}})$. This can be solved by typical solvers for nonlinear least-square problems.

5. Evaluation

5.1. Implementation

We implement the proposed LiDAR-inertial odometry and mapping system in C++ using ROS [26]. The three modules shown in Fig. 5 are structured as three individual nodes. The nonlinear optimization problem in (3) is solved using the Ceres Solver [27]. We use GTSAM [28] to perform factor graph optimization for rectifying the global pose graph at loop closures. The proposed system is developed with a focus on the Livox Horizon, thus named as LiLi-OM. It is, however, also applicable for

conventional LiDARs with mechanical spinning mechanisms due to its generic design for backend fusion. Therefore, two versions of the systems are deployed for evaluation: (1) The original LiLi-OM for the Livox Horizon with the proposed feature extraction approach from Sec. 3 and (2) its variant using the preprocessing module of [14] to extract features for conventional LiDARs.

In the following sections, we conduct extensive evaluations using public data sets (recorded using conventional LiDARs) and experiments (including data sets recorded by the Livox Horizon). Here, the LiDAR sampling frequency is 10 Hz.

5.2. Public data set

Existing public LiDAR-inertial data sets are all recorded using conventional mechanical spinning LiDARs. In this section, we deploy the variant of LiLi-OM using the feature extraction method of [14] to evaluate the proposed sensor fusion scheme. The following state-of-the-art LiDAR-based odometry systems are considered for comparison: A-LOAM⁹ (open-source version of LOAM [14]), LeGO-LOAM [15], LIO-mapping (abbreviated as LIOM) [19], LINS [20] and LIO-SAM [21]. Here, A-LOAM and LeGO-LOAM are LiDAR odometry systems. LIOM, LINS, and LIO-SAM use both LiDAR and IMU measurements.

We use the EU long-term data set (UTBM) [29], which provides two long urban navigation sequences recorded by a Velodyne HDL-32E and a six-axis IMU (100 Hz). LIO-SAM requires nine-axis IMU measurements. For that, we include the UrbanLoco and UrbanNav data sets [7], which are recorded using a Velodyne HDL-32E with an Xsens MTi-10 streaming nine-axis IMU readings at 100 Hz. For evaluation, the absolute position error (APE) of RMSE is calculated with reference to the recorded ground truth using [30].

Shown in Tab. 1, the proposed LiDAR-inertial fusion scheme (LiLi-OM) achieves the best tracking accuracy in real time for all sequences (denoted as bold font). LIO-SAM [21] requires nine-axis IMU readings for de-skewing and perform frontend odometry, thereby not applicable for the UTBM data sets. For the remaining sequences, LIO-SAM still shows worse tracking accuracy than LiLi-OM though it additionally exploits orientation measurements from a magnetometer. This mainly results from the unified fusion scheme of LiLi-OM where LiDAR and inertial measurements are directly fused. LIO-mapping loses tracking on UrbanNav data sets (denoted as ✗) and delivers very large drift for the first UTBM sequence. Moreover, it cannot run in real time with recommended configurations. LOAM also delivers large tracking errors on UTBM data sets as the implementation limits the iteration number in scan-matching for achieving real-time processing.

Table 1: APE (RMSE) for evaluation with public data sets

Dataset ¹	A-LOAM	LeGO-LOAM	LIOM	LINS	LIO-SAM	LiLi-OM
UTBM-1	479.51 m	17.12 m	468.75 m	16.90 m	–	8.61 m
UTBM-2	819.95 m	6.46 m	12.95 m	9.31 m	–	6.45 m
UL-1	2.39 m	2.22 m	2.53 m	2.27 m	2.54 m	1.59 m
UL-2	2.58 m	2.30 m	2.00 m	2.99 m	2.50 m	1.20 m
UN-1	11.20 m	2.70 m	✗	2.19 m	2.28 m	1.08 m
UN-2	12.70 m	4.15 m	✗	4.80 m	5.31 m	3.24 m

¹Abbreviations: UTBM-1: UTBM-20180719, UTBM-2: UTBM-20180418-RA (roundabout), UL-1: UrbanLoco-HK-20190426-1, UL-2: UrbanLoco-HK-20190426-2, UN-1: UrbanNav-HK-20190314, UN-2: UrbanNav-HK-20190428.

5.3. Experiment

To further test the performance of LiLi-OM for solid-state-LiDAR-inertial odometry and mapping in real-world scenarios, we set up a sensor suite composed of a Livox Horizon and an Xsens MTi-670 IMU. The total cost of the sensor suite is only about 1700 Euros (as for Q1 2020), which is much cheaper than conventional LiDAR-inertial setups.

⁹<https://github.com/HKUST-Aerial-Robotics/A-LOAM>

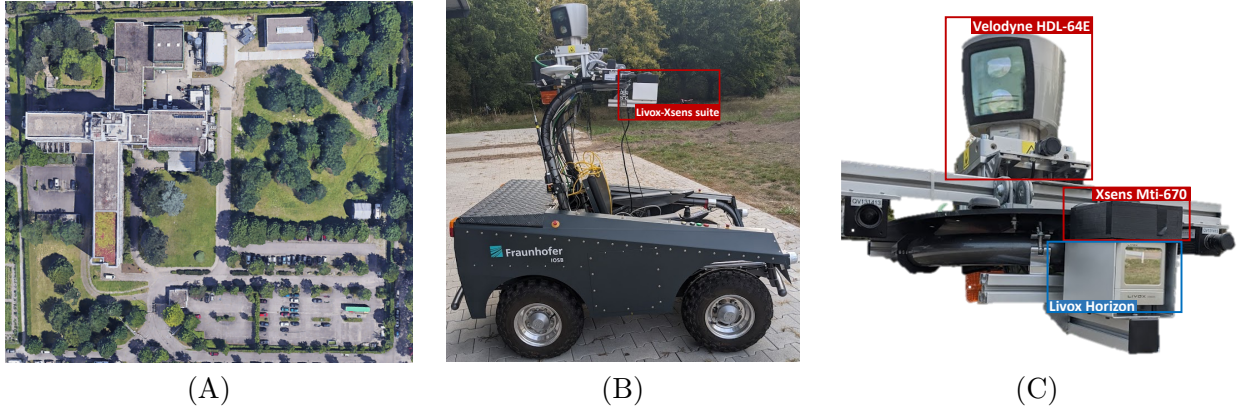


Figure 6: Experimental setup for FR-IOSB data set.

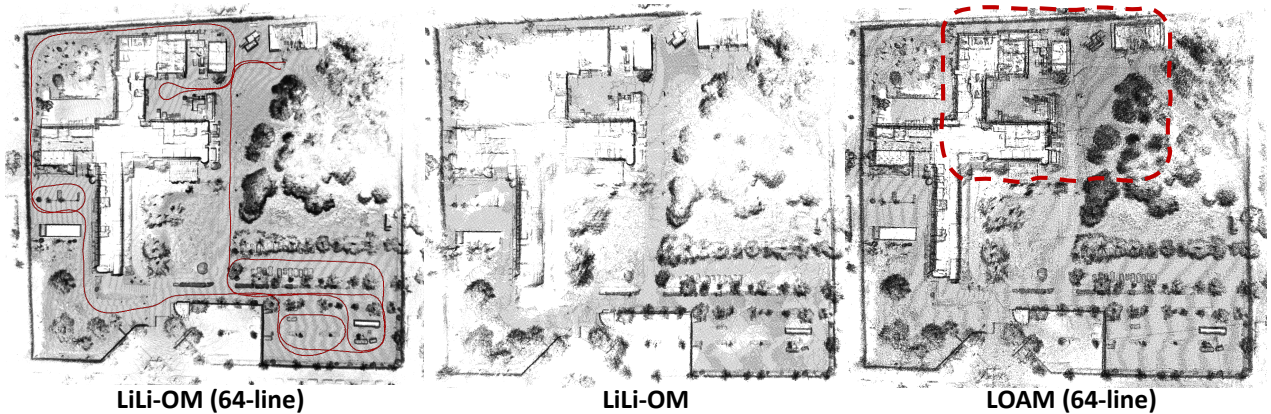


Figure 7: Mapping on FR-IOSB-Long. LOAM delivers inferior mapping accuracy than LiLi-OM, especially in dashed box.

5.3.1. FR-IOSB data set

Shown in Fig. 6-(B), a mobile platform is instrumented with the proposed Livox-Xsens suite. For comparison with high-end mechanical spinning LiDARs, we set up a Velodyne HDL-64E onboard and synchronize it with an Xsens MTi-G-700 IMU (around 150 Hz). A detailed setup of onboard sensors is shown in Fig. 6-(C). We recorded three sequences at the Fraunhofer IOSB campus of Fig. 6-(A): (1) FR-IOSB-Short recorded in structured scenario with short trajectory length, (2) FR-IOSB-Tree recorded in trees and bushes, and (3) FR-IOSB-Long of long trajectory length. We test both versions of LiLi-OM (for HDL-64E and Horizon).

For comparison, we run LOAM, LeGO-LOAM and Livox-Horizon-LOAM (LH-LOAM)¹⁰, an variant of LOAM adapted to the Livox Horizon. Note that this implementation also exploits IMU readings to handle motion distortion of LiDAR point cloud. Tab. 2 shows the end-to-end position error of the approaches. Results of best tracking accuracy for each sequence are all achieved by the two variants of LiLi-OM (denoted as bold font). Furthermore, we show the reconstructed map given by LOAM using the 64-line Velodyne LiDAR and maps from the two versions of LiLi-OM. The proposed fusion scheme enables accurate mapping results using both conventional and solid-state LiDARs.

¹⁰https://github.com/Livox-SDK/livox_horizon_loam

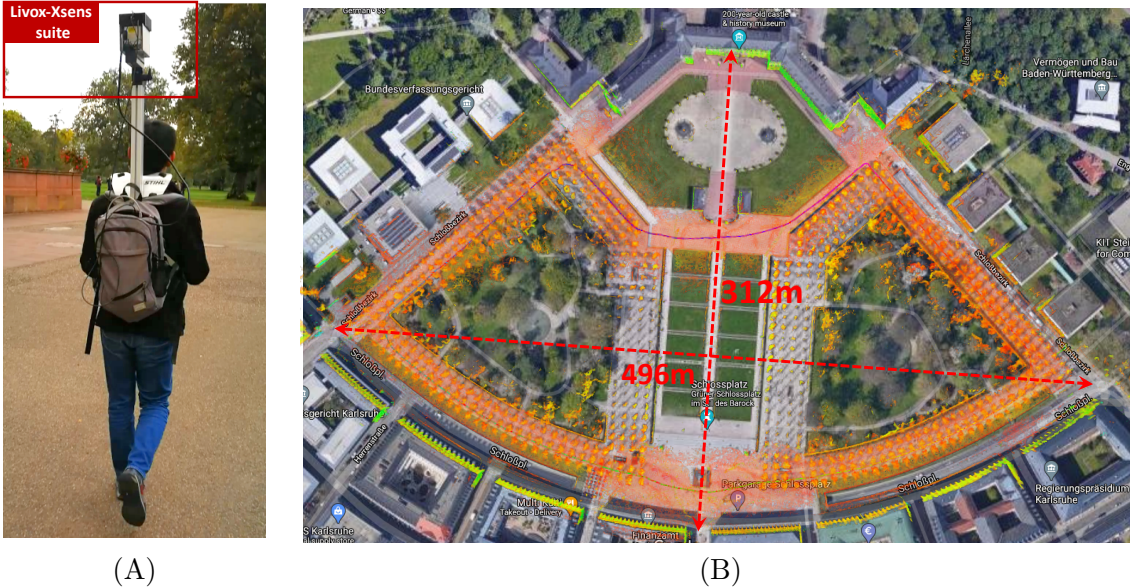


Figure 8: (A) Recording KA-Urban data sets using proposed sensor suite. (B) Result of Schloss-2 from LiLi-OM.

Table 2: End-to-end position error for FR-IOSB

Dataset	length	speed	LOAM	LH-LOAM	LeGO ¹	LiLi-OM ²	LiLi-OM
Short	0.49 km	2.15 m/s	0.78 m	5.04 m	0.25 m	0.34 m	0.25 m
Tree	0.36 km	1.12 m/s	0.21 m	0.13 m	78.22 m	< 0.1 m	< 0.1 m
Long	1.10 km	1.71 m/s	0.43 m	3.91 m	0.82 m	< 0.1 m	0.34 m

¹denotes LeGO-LOAM. ²adapted feature extraction module for Velodyne HDL-64E.

5.3.2. KA-Urban data set

The proposed Livox-Xsens sensor suite is further deployed onboard a backpack system for large-scale odometry and mapping in urban scenarios (shown in Fig. 8-(A)). Five sequences were recorded in the city of Karlsruhe, Germany and end-to-end locations were registered from satellite images. Besides LiLi-OM, we deactivate its loop closure module to evaluate its LiDAR-inertial odometry accuracy without correcting the global pose graph. Livox-Horizon-LOAM (LH-LOAM) is also run for comparison.

The resulted end-to-end errors of the three systems are collected in Tab. 3. With regard to pure odometry without corrections at loop closures, LiLi-OM (denoted as OL for open loop) delivers much less drift than LH-LOAM. When the loop closing function is activated, LiLi-OM shows very little drift. The mapping result from running LiLi-OM on sequence Schloss-1 is shown in Fig. 1 from different viewpoints. There, the Schloss Karlsruhe is digitalized in 3D point cloud with very high precision using the proposed Horizon-Xsens suite. We also show the result of running LiLi-OM on sequence Schloss-2 for an area of 496 m \times 312 m in Fig. 8-(B). The reconstructed map is globally consistent and is coherent to the underlying map from satellite imagery. We additionally show the results on sequence East, which was recorded while cycling through the streets in eastern Karlsruhe for a long trajectory. Though undergoing fast and dynamic motion, LiLi-OM delivers accurate odometry result and consistent map using the proposed low-cost sensor suite (shown in Fig. 9).

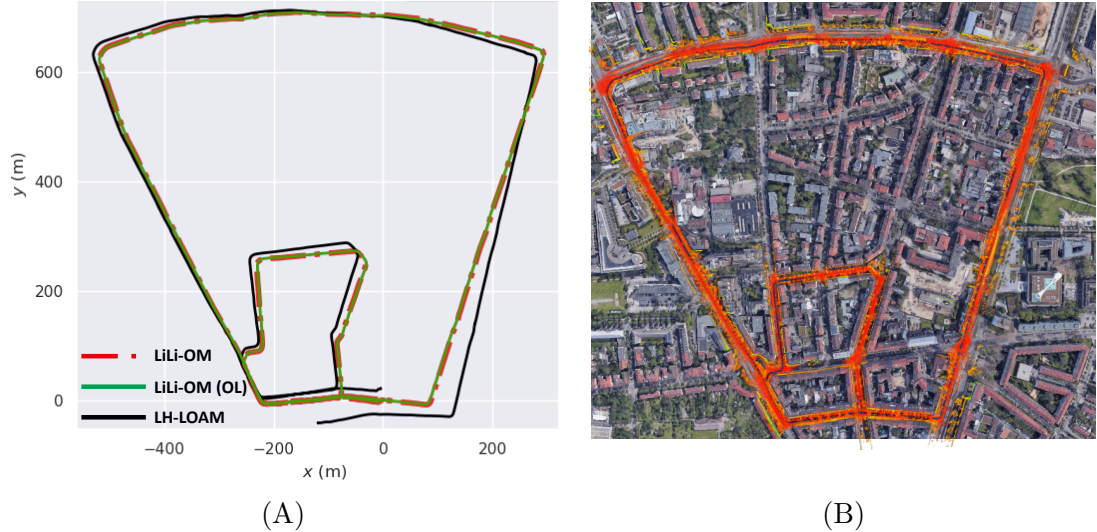


Figure 9: Evaluation results on KA-Urban-East. LiLi-OM gives accurate for odometry and mapping result.

Table 3: End-to-end position error for KA-Urban

Data Set	Length	Speed	LH-LOAM	LiLi-OM (OL)	LiLi-OM
Campus-1	0.50 km	1.43 m/s	1.47 m	1.11 m	0.13 m
Campus-2	0.20 km	1.57 m/s	0.40 m	0.21 m	0.19 m
Schloss-1	0.65 km	1.03 m/s	1.55 m	0.95 m	0.15 m
Schloss-2	1.10 km	1.49 m/s	8.34 m	4.41 m	0.08 m¹
East	3.70 km	3.11 m/s	109.62 m	15.66 m	1.28 m

¹trajectory ends at starting point.

5.4. Runtime

For all the data sets involved in the evaluation above, LiLi-OM runs in real time. As shown in Fig. 2, the proposed system is composed of three nodes performing preprocessing, LiDAR odometry, and backend fusion. In Tab. 4, we collect the average runtime of running each node of LiLi-OM for representative sequences in the evaluation. All evaluations are done on a laptop (Intel Core i5-7300HQ CPU, 8GB RAM).

The preprocessing node mainly performs feature extraction and the LiDAR-odometry module provides fast motion estimation for selecting keyframes and de-skewing purposes. They are designed to be lightweight. In the backend node, LiDAR-inertial measurements are fused in the keyframe-based sliding windows via optimization. For all sequences recorded by different LiDARs (including Velodyne HDL-64E) in various scenarios, the proposed system shows real-time performance (w.r.t. the LiDAR sampling frequency).

Table 4: Runtime of LiLi-OM per frame

Dataset	Preprocessing	LiDAR Odometry	Backend Fusion
UTBM-2	12.72 ms	22.29 ms	50.27 ms
UL-1	13.31 ms	23.71 ms	57.62 ms
FR-IOSB-Large (64-line)	30.14 ms	16.71 ms	60.92 ms
FR-IOSB-Large	9.99 ms	22.69 ms	58.86 ms
KA-Urban-Schloss-2	10.21 ms	27.15 ms	54.56 ms
KA-Urban-East	11.76 ms	25.30 ms	41.81 ms

6. Conclusion

In this work, we propose a novel sensor fusion method for real-time LiDAR-inertial odometry and mapping. A keyframe-based hierarchical scheme is established for directly fusing LiDAR and (pre-integrated) IMU measurements via sliding window optimization. Given the optimized keyframe states, regular-frame poses are obtained via factor graph optimization. The proposed LiDAR-inertial odometry and mapping system is universally applicable for both conventional LiDARs and solid-state LiDARs of small FoVs. For the latter use case, a novel feature extraction method is designed for the irregular and unique scan pattern of Livox Horizon, a newly released spinning free, solid-state LiDAR with much lower price than conventional 3D LiDARs. We conduct evaluations on both public data sets of conventional LiDARs and experiments using the Livox Horizon. Results show that the proposed system is real-time capable and delivers superior tracking and mapping accuracy over state-of-the-art LiDAR/LiDAR-inertial odometry systems. The proposed system, LiLi-OM, is featured as a cost-effective solution of high-performance LiDAR-inertial odometry and mapping using solid-state LiDAR.

There is still much potential to exploit for the proposed system. The deployed Livox-Xsens suite is lightweight and LiLi-OM is developed for universal egomotion estimation (not only for planar motion as [15]). Thus, it should be, for instance, tested onboard unmanned aerial vehicles in applications such as autonomous earth observation or environmental modeling coping with aggressive six-DoF egomotion. For large-scale odometry and mapping with limited computational resources, advanced map representations can be employed to improve memory as well as runtime efficiency. Potential options include volumetric mapping using TSDF (Truncated Signed Distance Fields) [4] or mapping with geometric primitives (especially in man-made environment [31]).

Acknowledgment

The work is supported by German Research Foundation (DFG) under grant HA 3789/16-1. We would like to thank Thomas Emter from Fraunhofer IOSB for providing the robot platform and assistance in recording the FR-IOSB data set.

References

- [1] J. Engel, J. Sturm, and D. Cremers, "Camera-Based Navigation of a Low-Cost Quadcopter," in *Proceedings of the 2008 IEEE/RSJ International Conference on Intelligent Robots and Systems (IROS 2012)*, Vilamoura, Portugal, Oct. 2012.
- [2] M. Bloesch, M. Burri, S. Omari, M. Hutter, and R. Siegwart, "Iterated Extended Kalman Filter Based Visual-Inertial Odometry Using Direct Photometric Feedback," *The International Journal of Robotics Research*, vol. 36, no. 10, pp. 1053–1072, 2017.
- [3] O. Kähler, V. A. Prisacariu, J. P. C. Valentin, and D. W. Murray, "Hierarchical Voxel Block Hashing for Efficient Integration of Depth Images," *IEEE Robotics and Automation Letters*, vol. 1, no. 1, pp. 192–197, 2016.
- [4] V. Reijgwart, A. Millane, H. Oleynikova, R. Siegwart, C. Cadena, and J. Nieto, "Voxgraph: Globally Consistent, Volumetric Mapping Using Signed Distance Function Submaps," *IEEE Robotics and Automation Letters*, vol. 5, no. 1, pp. 227–234, Jan 2020.
- [5] S. Bultmann, K. Li, and U. D. Hanebeck, "Stereo Visual SLAM Based on Unscented Dual Quaternion Filtering," in *Proceedings of the 22nd International Conference on Information Fusion (Fusion 2019)*, Ottawa, Canada, July 2019.
- [6] A. Geiger, P. Lenz, C. Stiller, and R. Urtasun, "Vision Meets Robotics: The KITTI Dataset," *The International Journal of Robotics Research*, vol. 32, no. 11, pp. 1231–1237, 2013.
- [7] W. Wen, Y. Zhou, G. Zhang, S. Fahandezh-Saadi, X. Bai, W. Zhan, M. Tomizuka, and L.-T. Hsu, "Urbanloco: A Full Sensor Suite Dataset for Mapping and Localization in Urban Scenes," in *Proceedings of the 2020 International Conference on Robotics and Automation (ICRA 2020)*, Paris, France, May 2020, pp. 2310–2316.
- [8] F. Pomerleau, F. Colas, R. Siegwart, and S. Magnenat, "Comparing ICP Variants on Real-World Data Sets," *Autonomous Robots*, vol. 34, no. 3, pp. 133–148, Feb. 2013.
- [9] Y. Chen and G. Medioni, "Object Modelling by Registration of Multiple Range Images," *Image and Vision Computing*, vol. 10, no. 3, pp. 145–155, 1992.
- [10] A. Segal, D. Haehnel, and S. Thrun, "Generalized-ICP," in *Proceedings of the 2009 Robotics: Science and Systems (RSS 2009)*, vol. 2, no. 4, Edinburgh, UK, June 2009.

- [11] R. B. Rusu, G. Bradski, R. Thibaux, and J. Hsu, “Fast 3D Recognition and Pose Using the Viewpoint Feature Histogram,” in *Proceedings of the 2010 IEEE/RSJ International Conference on Intelligent Robots and Systems (IROS 2010)*, 2010, pp. 2155–2162.
- [12] Y. Li and E. B. Olson, “Structure Tensors for General Purpose LIDAR Feature Extraction,” in *Proceedings of the 2011 IEEE International Conference on Robotics and Automation (ICRA 2011)*, 2011, pp. 1869–1874.
- [13] G. Kim and A. Kim, “Scan Context: Egocentric Spatial Descriptor for Place Recognition within 3D Point Cloud Map,” in *Proceedings of the 2018 IEEE/RSJ International Conference on Intelligent Robots and Systems (IROS 2018)*, Madrid, Spain, October 2018, pp. 4802–4809.
- [14] J. Zhang and S. Singh, “LOAM: Lidar Odometry and Mapping in Real-time,” in *Proceedings of the 2014 Robotics: Science and Systems (RSS 2014)*, vol. 2, no. 9, Berkeley, California, USA, July 2014.
- [15] T. Shan and B. Englot, “LeGO-LOAM: Lightweight and Ground-Optimized Lidar Odometry and Mapping on Variable Terrain,” in *Proceedings of the 2018 IEEE/RSJ International Conference on Intelligent Robots and Systems (IROS 2018)*, Madrid, Spain, October 2018, pp. 4758–4765.
- [16] I. Bogoslavskyi and C. Stachniss, “Fast Range Image-Based Segmentation of Sparse 3D Laser Scans for Online Operation,” in *Proceedings of the 2016 IEEE/RSJ International Conference on Intelligent Robots and Systems (IROS 2016)*, 2016, pp. 163–169.
- [17] J. Tang, Y. Chen, X. Niu, L. Wang, L. Chen, J. Liu, C. Shi, and J. Hyypää, “LiDAR Scan Matching Aided Inertial Navigation System in GNSS-Denied Environments,” *Sensors*, vol. 15, no. 7, pp. 16 710–16 728, 2015.
- [18] C. Le Gentil, T. Vidal-Calleja, and S. Huang, “IN2LAAMA: Inertial Lidar Localization Autocalibration and Mapping,” *IEEE Transactions on Robotics*, pp. 1–16, 2020.
- [19] H. Ye, Y. Chen, and M. Liu, “Tightly Coupled 3D Lidar Inertial Odometry and Mapping,” in *Proceedings of the 2019 International Conference on Robotics and Automation (ICRA 2019)*, Montreal, Canada, May 2019, pp. 3144–3150.
- [20] C. Qin, H. Ye, C. E. Pranata, J. Han, S. Zhang, and M. Liu, “LINS: A Lidar-Inertial State Estimator for Robust and Efficient Navigation,” in *Proceedings of the 2020 International Conference on Robotics and Automation (ICRA 2020)*, Paris, France, May 2020.
- [21] T. Shan, B. Englot, D. Meyers, W. Wang, C. Ratti, and R. Daniela, “LIO-SAM: Tightly-coupled Lidar Inertial Odometry via Smoothing and Mapping,” in *Proceedings of the 2020 IEEE/RSJ International Conference on Intelligent Robots and Systems (IROS 2020)*, Las Vegas, Nevada, USA, Oct 2020.
- [22] M. Kaess, H. Johannsson, R. Roberts, V. Ila, J. J. Leonard, and F. Dellaert, “iSAM2: Incremental Smoothing and Mapping Using the Bayes Tree,” *The International Journal of Robotics Research*, vol. 31, no. 2, pp. 216–235, 2012.
- [23] J. Lin and F. Zhang, “Loam Livox: A Fast, Robust, High-Precision LiDAR Odometry and Mapping Package for LiDARs of Small FoV,” in *Proceedings of the 2019 International Conference on Robotics and Automation (ICRA 2019)*, Montreal, Canada, May 2019, pp. 3126–3131.
- [24] S. Leutenegger, S. Lynen, M. Bosse, R. Siegwart, and P. Furgale, “Keyframe-Based Visual-Inertial Odometry Using Nonlinear Optimization,” *The International Journal of Robotics Research*, vol. 34, no. 3, pp. 314–334, 2015.
- [25] T. Qin, P. Li, and S. Shen, “VINS-Mono: A Robust and Versatile Monocular Visual-Inertial State Estimator,” *IEEE Transactions on Robotics*, vol. 34, no. 4, pp. 1004–1020, 2018.
- [26] M. Quigley, B. Gerkey, K. Conley, J. Faust, T. Foote, J. Leibs, E. Berger, R. Wheeler, and A. Ng, “ROS: An Open-source Robot Operating System,” *ICRA Workshop on Open Source Software*, vol. 3, no. 3.2, p. 5, 2009.
- [27] S. Agarwal, K. Mierle, and Others, “Ceres Solver,” <http://ceres-solver.org>.
- [28] F. Dellaert, “Factor Graphs and GTSAM: A Hands-on Introduction,” Georgia Institute of Technology, Tech. Rep., 2012.
- [29] Z. Yan, L. Sun, T. Krajník, and Y. Ruichek, “EU Long-term Dataset with Multiple Sensors for Autonomous Driving,” in *Proceedings of the 2020 IEEE/RSJ International Conference on Intelligent Robots and Systems (IROS 2020)*, Las Vegas, Nevada, USA, Oct 2020.
- [30] M. Grupp, “evo: Python Package for the Evaluation of Odometry and SLAM,” <https://github.com/MichaelGrupp/evo>, 2017.
- [31] H. Möls, K. Li, and U. D. Hanebeck, “Highly Parallelizable Plane Extraction for Organized Point Clouds Using Spherical Convex Hulls,” in *Proceedings of the 2020 IEEE International Conference on Robotics and Automation (ICRA 2020)*, Paris, France, May 2020.